

# Artificial Intelligence Assisted Inversion (AIAI): Quantifying the Spectral Features of <sup>56</sup>Ni of Type Ia Supernovae

XINGZHUO CHEN,<sup>1</sup> LIFAN WANG,<sup>1</sup> LEI HU,<sup>2</sup> AND PETER J. BROWN<sup>1</sup>

<sup>1</sup>*George P. and Cynthia Woods Mitchell Institute for Fundamental Physics & Astronomy,  
Texas A. & M. University, Department of Physics and Astronomy, 4242 TAMU, College Station, TX 77843, USA*

<sup>2</sup>*Purple Mountain Observatory, Nanjing 210008, People's Republic of China*

(Received January 1, 0000; Revised January 1, 0000; Accepted January 1, 0000)

Submitted to ApJ

## ABSTRACT

Following our previous study of Artificial Intelligence Assisted Inversion (AIAI) of supernova analyses (Chen et al. 2020), we train a set of deep neural networks based on the one-dimensional radiative transfer code TARDIS (Kerzendorf & Sim 2014) to simulate the optical spectra of Type Ia supernovae (SNe Ia) between 10 and 40 days after the explosion. The neural networks are applied to derive the mass of <sup>56</sup>Ni in velocity ranges well above the photosphere for a sample of 153 well-observed SNe Ia. Many SNe have multi-epoch observations for which the decay of the radioactive <sup>56</sup>Ni can be tested quantitatively. The <sup>56</sup>Ni mass derived from AIAI using the observed spectra as input for the sample is found to agree with the theoretical <sup>56</sup>Ni decay rate. The AIAI reveals a spectral signature near 3890 Å which can be identified as being produced by multiple Ni II lines between 3950 and 4100 Å. The mass deduced from AIAI is correlated to the light-curve shapes of SNe Ia, with the SNe Ia with broader light curves showing larger <sup>56</sup>Ni mass in the envelope. AIAI enables spectral data of SNe to be quantitatively analyzed under theoretical frameworks based on well-defined physical assumptions.

## 1. INTRODUCTION

Type Ia supernovae (SNe Ia) are used for cosmological distance measurements based on empirical relations between their light curve shapes and luminosities (Phillips 1993; Guy et al. 2005; Wang et al. 2003a; Rubin et al. 2013; Yang et al. 2022a; Aldoroty et al. 2022). These relations are consistent with theoretical models of the thermonuclear explosion of a white dwarf close to the Chandrasekhar mass limit ( $1.4 M_{\odot}$ ). Although several three-dimensional SNe Ia explosion simulations could provide comparable photometric and spectroscopic features compared to the observed SNe Ia light curves and spectral sequences (e.g., Bulla et al. 2016; Wilk et al. 2017; Townsley et al. 2019), the first principle hydrodynamics, nucleosynthesis, and radiative transfer simulation results of SNe Ia are extremely expensive to calculate and still far from the level of precision that matches those of observations.

Hydrodynamic and nucleosynthesis processes are only significant in the first  $\sim 100$  seconds (Röpke 2005). Thereafter the supernova (SN) ejecta expand homologously and the observed optical spectra and light curves are governed by radiative transfer and the thermal state of the ejecta. Modeling the radiative transfer process is essential in the estimates of the density profiles and elemental abundances of the SN ejecta so as to put constraints on the SN explosion mechanisms. Several programs have been developed for the calculations of synthetic spectra. The simplest is the SYNOW code (Parent et al. 2010; Thomas et al. 2011) which directly uses line opacity data to generate synthetic spectra and has been widely used in spectral line identifications. Hydra (Hoefflich et al. 1996), PHOENIX (Hauschildt & Baron 2006) and CMFGEN (Hillier & Miller 1998) are more advanced simulation programs that allow for more accurate modeling through finite element approach. Programs using the Monte-Carlo method have also been developed for spectral simulation (e.g., SEDONA (Kasen et al. 2006), ARTIS (Kromer & Sim 2009)) and have been used for spectropolarimetry calculations (Höflich

1991; Kasen et al. 2003; Bulla et al. 2015; Livneh & Katz 2022). In spectropolarimetry modeling, 3-D effects, non-local thermodynamic equilibrium (NLTE), and time-dependent radiative transfer effects are important. Among these codes, TARDIS (Kerzendorf & Sim 2014) is a one-dimensional, time-independent Monte-Carlo radiative transfer program with approximate NLTE treatment of atomic processes.

Model-based analyses enable "abundance tomography" of the SN ejecta (e.g., Hoefflich et al. 1996; Stehle et al. 2005). The Artificial Intelligence Assisted Inversion (AIAI) of SN Ia spectra (Chen et al. 2020) trains a set of neural networks (NNs) based on the simulated spectra using the radiative transfer program TARDIS (Kerzendorf & Sim 2014) to derive the elemental abundances of several well-observed SNe Ia at around 20 days after the explosion. Kerzendorf et al. (2020) used a NN to accelerate the calculation of the radiative transfer program, and suggest that the method can be used for SN ejecta structure estimate based on a nested sampling algorithm.

Among the 23 elements (from number 6 element C, to number 28 element Ni) that play significant roles in the nucleosynthesis process of the SNe Ia,  $^{56}\text{Ni}$  stands out for two reasons. Firstly, the decay chain of  $^{56}\text{Ni}$  is the major energy source that powers the radiative process of SN Ia. The observed light curves can be used to determine the total  $^{56}\text{Ni}$  masses of SNe Ia (e.g. Arnett 1982; Woosley et al. 2007; Khatami & Kasen 2019). Secondly, the spatial distribution of  $^{56}\text{Ni}$  in SN ejecta is directly related to the SN explosion mechanism (e.g., Piro et al. 2010; Piro & Morozova 2016)). A problem is that unlike the Si II 6355Å and Ca II 8542Å lines, which are strong lines that are clearly distinguishable from other lines, the spectral lines of  $^{56}\text{Ni}$  are blended and cannot be easily measured from the observed SN Ia spectra around the maximum. Childress et al. (2015) use Co III  $\lambda$ 5893 emission line in the nebular spectra of SNe Ia to estimate the mass before the radioactive decay of  $^{56}\text{Ni}$ . The AIAI approach has the distinct advantage that the line measurements do not rely strongly on any single spectral features. With a large enough training set, it can derive optimal estimates of the physical parameters with the entire observed spectra contributing to the reliability of all the parameters.

In this paper, we present a set of NNs and apply them to a sample of well-observed SNe Ia. The NNs are trained on the simulated spectra using TARDIS. Using the NN predicted SN ejecta structure, we identify a correlation between the spectral feature around 3950Å of SNe Ia spectra around B-band maximum time and the  $^{56}\text{Ni}$  mass in the SN ejecta. The paper is structured

as follows: Section 2 introduces the training dataset, the NN architecture, and the spectral sequence fitting pipeline. Section 4 shows the results of the spectral line measurement and the Ni mass measurements. Section 5 gives the conclusions. The code for this research is available at <https://github.com/GeronimoChen/DLTD>.

## 2. METHOD

### 2.1. TARDIS spectral calculation

In TARDIS calculation, SN ejecta is assumed to be spherically symmetric and expands homogeneously after the explosion. To avoid the computationally demanding time-dependent photon diffusion calculation, a simple approximation of the photosphere with a black-body emission spectrum at the inner boundary of SN ejecta is adopted. Given an SN ejecta structure, a target luminosity, a time after the explosion, and an inner boundary velocity, TARDIS can calculate a spectrum in  $\sim 1$  CPU hour.

The model spectra are calculated using the code TARDIS (version 3.0-dev3448). To set up the models, we use dilute local thermodynamic equilibrium (`dilute-lte`) Lucy (1999) approximation to calculate the atomic level population, nebular approximation (`nebular`) Mazzali & Lucy (1993) to calculate the ionization fraction, `macroatom` Lucy, L. B. (2002, 2003) to calculate the atomic level transition, `detailed` to calculate the black-body radiative rates. TARDIS uses an iterative algorithm (Lucy, L. B. 2003) to calculate a self-consistent SN temperature profile. As in our previous work on AIAI of SNe Ia spectra Chen et al. (2020) (Hereafter XLL20), the step of temperature iterations is set to 15, with the damping parameters being: (`type:damped. damping_constant:1 threshold:0.05. fraction:0.8. hold.iterations:3. t_inner_damping_constant:1`). The temperature calculation setup in our research does not return a converged temperature profile, but the final temperature profile can be modified by changing the target luminosity and the location of the inner boundary. We adopt this configuration for its flexibility in the temperature calculation which is necessary when the observed and the simulated spectra are compared quantitatively.

### 2.2. Simulated Spectral Library

In this section, we parameterize the supernova ejecta models based on the "IG" model in XLL20 Chen et al. (2020), and randomly sample the parameter space to create a supernova ejecta structure library.

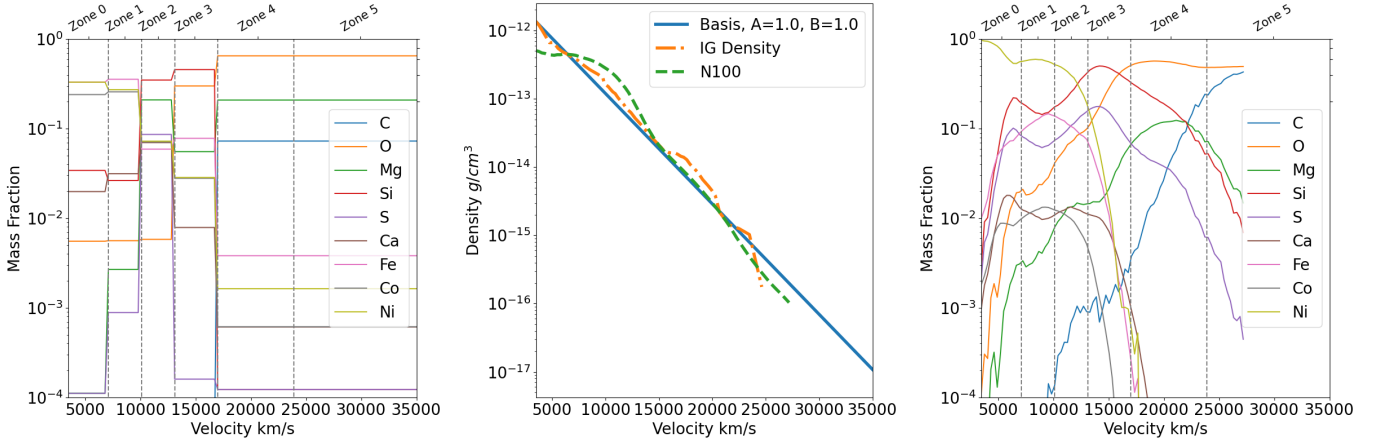


**Figure 1.** Left: The elemental abundance of the reference model. The label of zones are shown on the top of the panel, and the zone boundaries are marked by the grey dashed lines. Middle: The density structure of the reference model with  $A = 1$  and  $B = 1$  in Equation 1 used in this paper (blue line), the density structure in XLL20 (Chen et al. 2020) (orange dash-dotted line), and the density structure of the N100 model (green dashed line). The densities shown are at 11.5741 days after the explosion. Right panel: the elemental abundance structure of the N100 model.

We treat the SN ejecta density profile as a power-law relation shown below:

$$\rho(v) = 4.712 \times 10^{-14} \left( \frac{t}{11.5741 \text{ days}} \right)^{-3} A \cdot 0.689 \frac{(v - 12500 \text{ km/s})^B}{1000 \text{ km/s}} \text{ g/cm}^3, \quad (1)$$

where  $A$  and  $B$  are dimensionless parameters for the density profile,  $v$  is the expansion velocity, and  $t$  is the time after explosion. When  $A = 1$  and  $B = 1$ , the density profile is similar to the "IG" model in XLL20 (Chen et al. 2020) and serves as the reference density profile in this paper. A comparison between the density profiles is shown in Figure 1.

We divide the SN ejecta into 6 discrete zones in the velocity space. The elemental abundance is assumed to be constant inside a zone. There is no layer above 24000 km/s in the XLL20; we extrapolate the high-velocity component from the "IG" model in XLL20 (Chen et al. 2020) to serve as the reference elemental abundance in this paper. The elemental abundance structure and the density profile of the N100 model from (Röpke et al. 2012) are also shown in Figure 1 for comparison.

The parameters for generating the spectral library include:

- The density profile parameterized by  $A$  and  $B$  (see Equation 1):  $A$  and  $B$  are drawn from uniform distributions between  $[0.2, 2]$  and  $[0, 2]$ , respectively.
- The abundance of 23 elements in 6 zones of the ejecta structure: The abundance of an element in a given zone is drawn from a Gaussian distribution in the logarithmic space  $N(\mu, \sigma^2)$ , where  $\mu$  is the log of the abundance of the reference elemental

abundance structure, and  $\sigma$  is set to be 0.5 for all elements. Moreover, the sum of the elemental abundance in each zone is conserved to be 1.

- The time after the explosion: The time after the explosion is drawn from a uniform distribution in  $[10, 40]$  days.
- The supernova luminosity between 6500 Å and 7500 Å in units of  $\log_{10}(L_{\odot})$  and the location of the inner boundary: To set the parameter ranges of the SN luminosity and the location of the photosphere, we first use the reference ejecta structure (with  $A = B = 1$  in Equation 1) and the extrapolated "IG" abundance structure (from Chen et al. 2020) to calculate a spectral sequence between 10 days and 40 days after the explosion, with varying target luminosities and inner boundary velocities. By comparing the simulated spectra with the observed SNe Ia spectral energy distribution (e.g., Hsiao et al. 2007; Hu et al. 2022), we determine the lower and upper limits of the target luminosities and the locations of the inner boundary at different epochs after the explosion, the results are shown in Table 1.

When generating spectra for the spectral library to be used for neural network training, we sample the day after SN explosion from a uniform distribution in  $[10, 40]$ , then sample a target luminosity in logarithmic space from the uniform distribution between  $[L_{min}, L_{max}]$ , where  $L_{min}$  and  $L_{max}$  are taken from Table 1 with linear interpolations for days not included in the Table. The inner boundary velocity is also sampled from the uni-

Time (days)	Luminosity ( $\log_{10}(L_{\odot})$ )	Velocity (km/s)
10	8.2-8.35	10500-13000
12	8.3-8.4	10000-13000
14	8.4-8.5	9000-12000
16	8.5-8.6	7800-10000
18	8.5-8.7	7000-8200
20	8.55-8.7	6400-7500
22	8.55-8.65	5700-6700
24	8.5-8.65	5200-6200
26	8.47-8.62	4500-5800
28	8.42-8.6	4300-5100
30	8.38-8.52	4000-4900
32	8.3-8.5	3750-4700
34	8.15-8.45	3500-4700
36	8.1-8.35	3500-4700
38	8.0-8.3	3500-4700
40	7.8-8.2	3500-4700

**Table 1.** The inner boundary velocity and the luminosity range to generate the spectral library.

form distribution in  $[V_{min}, V_{max}]$ , where  $V_{min}$  and  $V_{max}$  are linearly interpolated from Table 1.

The wavelength range of the model spectra is between 2000 and 10000 Å with a total of 2000 wavelength bins. Each wavelength bin is separated by a frequency difference of  $5.9958 \times 10^{11}$  Hz. A total of 108,389 ejecta models and their corresponding spectra are calculated to form the spectral training set for building the NNs.

### 2.3. Neural Network

A typical NN consists of an input layer, an output layer, and multiple hidden layers. The input layer receives data as input tensors, then the tensors are processed by the hidden layers, and finally output to the output layer. Different types of layers, representing different mathematical calculations, can be used in the hidden layers. For example, the convolution layer convolves the data tensor with a convolution core, the activation layer applies a non-linear function onto the data tensor, pooling layer reduces the size of the data tensor by binning the adjacent data with the maximum values or the average values, fully-connected layer multiplies a matrix to the input tensor (for a review, see [Lecun et al. \(2015\)](#)).

The training target of a neural network is to provide predictions ( $y_{pred}$ ) over a variable of our interest that is close to the truth ( $y_{true}$ ), from the given information ( $X$ ). Initially, the trainable parameters (i.e. the convolution core in the convolution layers, and the matrix in the fully-connected layers, all denoted as  $w$ ) are

randomly assigned. The neural network then calculates the output ( $y_{pred}$ ) using the known information  $X$  as input, and a loss function (i.e. Mean Squared Error:  $Loss = Mean(y_{true} - y_{pred})^2$ ) is calculated to evaluate the performance of prediction. The trainable parameters are updated with respect to the gradient  $\partial L / \partial w$  and a pre-defined learning rate, to minimize the loss function. For computational efficiency, the dataset is separated into batches, and the trainable parameters are updated at each batch. The neural network will browse the data set multiple times, one browse is defined as one epoch.

Here we have adopted the deep ensemble NNs ([Lakshminarayanan et al. 2016](#)) which has the ability to make predictions and prediction uncertainties simultaneously. Comparing to typical NNs such as AlexNet ([Krizhevsky et al. 2012](#)) and VGG16 ([Simonyan & Zisserman 2014](#)), the output of deep ensemble NNs is not the just the prediction value, but the prediction mean  $\mu$  together with the prediction error  $\sigma$ , assuming a Gaussian noise distribution. The loss function is:

$$Loss = Mean \left( \ln(\sigma(x)) + \frac{(y_{true,i} - \mu(x))^2}{\sigma(x)^2} \right), \quad (2)$$

where  $x$  is the input information of the neural network which includes the spectrum, the time after the explosion, and the density parameters;  $\mu$  and  $\sigma$  are written in function forms to represent the neural network.

We use the multi-residual NNs ([Abdi & Nahavandi 2016](#); [Chen et al. 2020](#)) for the NN architecture. In brief, we introduce a block structure with two convolution layers, a batch normalization layer, and an activation layer, and repeat the block structure 7 times. The input of the block structure is the sum of the output of all the previous block structures and the input of the first block structure. Moreover, the NN has two inputs, the 2000-element array `input_1` that receives the input spectra with 2000 pixels from 2000 to 10000 Å, and the 3-element array `input_2` that receives the density parameters  $A$  and  $B$  shown in Equation 1 and the time after the explosion. We use the Scaled Exponential Linear Unit (SELU) function as the activation function for all the hidden layers:

$$selu(x) = \begin{cases} scale \times x, & (x > 0) \\ scale \times \alpha \times (e^x - 1), & (x \leq 0), \end{cases} \quad (3)$$

where  $scale = 1.05070098$  and  $\alpha = 1.67326324$ . The detailed architecture is shown in the [online material](#).

Among all the 108389 spectra, 80% of them are assigned to the training set, 20% are included in the testing set. The training dataset will be used to update the

trainable parameters, while the testing dataset is only used to monitor the loss function after every epoch.

Note that not all the observed spectral data cover the entire UV-optical-IR wavelength from 2000 to 10000 Å. Data augmentation is applied to the dataset to cope with the problem. In this augmentation method, we duplicate both the training and the testing data set by making 5 copies of them. The spectra in the first copies of the training and the testing data set remain the same as the spectra in the original spectral library. For each spectrum in the other 4 copies, we randomly select an observational facility (telescope and instrument) that was used to acquire the spectral observations of SNe in the WISEREP database, then apply the wavelength coverage of that facility onto the spectrum. Furthermore, each spectrum is normalized by dividing the spectrum by the average pixel value, in order to avoid overflow in the NNs.

We used the `adam` algorithm (Kingma & Ba 2014) to update the trainable parameters, with a batch size of 200. The training process consists of two phases with different learning rates. In the first phase, the learning rate is 0.00003 and decays  $10^{-6}$  per batch. The loss in Equation 2 is calculated on the training data set and the testing data set respectively after every epoch. When the loss on the testing data set does not decrease in the recent 10 epochs, we cease the first phase and keep the model with the smallest loss for the second phase. In the second phase, the learning rate is 0.000003 and decays  $10^{-6}$  per batch. We also monitor the loss on the training data set and the testing data set every epoch. When the loss on the testing data set does not decrease in the recent 10 epochs, we cease the training and keep the NN model with the smallest loss on the testing data set.

We trained 7 sets of NNs in total, the first six NNs are designed to predict 30 elemental abundances (from H to Zn) in Zones 0 – 5, and the seventh NN is designed to predict the inner boundary velocity and the luminosity. The seventh NN has two outputs, while the other six NNs have 30 outputs. The loss on the testing data set is shown in Figure 2 and Figure 3.

#### 2.4. Density Estimation

In XLL20 (Chen et al. 2020), we applied a grid search method to determine the inner boundary velocity and the target luminosity, while applying a rigid density profile for both the model spectral training set and density profile for applications to the observed spectra. With the increased number of SNe to fit, and the two extra density parameters to be determined, the grid search is too computationally expensive for the current research.

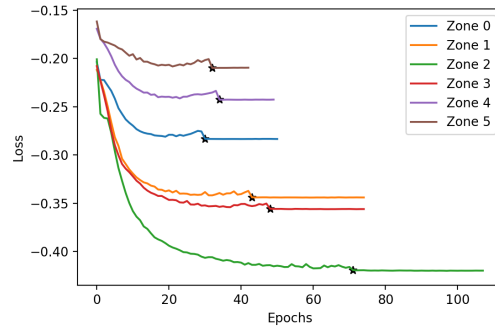


**Figure 2.** The learning curves of the 6 NNs for elemental abundance predictions in Zones 0 – 5, showing the losses on the testing data set at different epochs. The black stars show the starting points of the second phase in the training process. The losses for zones 0 to 5 are shown with blue, orange, green, red, purple, and brown lines, respectively.

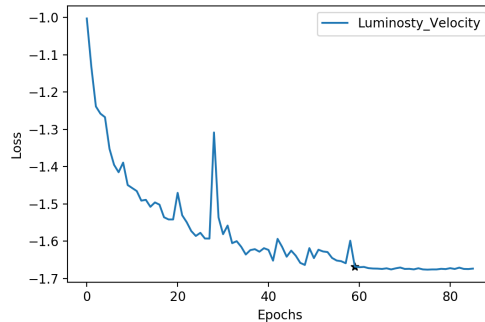


**Figure 3.** The learning curve of the NN predicting the luminosity and inner boundary velocity. The line shows the losses with the testing dataset at different epochs. The black star shows the beginning of the second phase in the training process.

A more efficient search algorithm is designed for this study. For an observed spectral sequence of an SN Ia, we first use the NNs to predict the time sequences of the elemental abundances, the luminosities, and the velocities of the inner boundary for a given grid of density parameters and the phase of each spectrum. We use TARDIS to re-calculate the simulated spectral sequences for this density parameter grid. The simulated spectral sequences are compared with the observed spectral sequence using the mean squared error as the merit function:

$$MSE(A, B) = \sum_i \sum_{\lambda} (F_{i,obs}(\lambda) - F_{i,sim}(\lambda, A, B))^2, \quad (4)$$

where  $i$  is the index of spectra in the spectral sequence,  $F_{i,obs}(\lambda)$  is the  $i$ -th observed spectrum,  $F_{i,sim}(\lambda, A, B)$  is the  $i$ -th spectra in the simulated spectral sequence

using the density parameters  $A$  and  $B$ . The simulated spectra are masked according to their wavelength coverage of the observed spectra with the missing wavelength regions set to have zero weights and normalized by dividing the spectra by the average pixel value. The observed spectra are re-sampled with the wavelength grid of the simulated spectra, and also normalized by their average pixel values.

Equation 4 has only two free parameters  $A$  and  $B$  to be determined. The best  $A$  and  $B$  parameters that minimize Equation 4 are calculated through a grid search but still involve a large number of spectral model computations. We have applied the following method for further improvement. The method has 4 iterations, each iteration calculates the spectral sequence in a different sub-grid. In the first iteration, the sub-grid is set to be  $A = [0.5, 1.1, 1.7]$ ,  $B = [0.5, 1.1, 1.7]$ . In the second iteration, the sub-grid is specified as  $A = [a - 0.2, a, a + 0.2]$ ,  $B = [b - 0.2, b, b + 0.2]$ , where  $a$  and  $b$  are the parameters set with the smallest mean squared error from the first iteration. In the third iteration, the sub-grid is replaced by  $A = [a - 0.2, a, a + 0.2]$ ,  $B = [b - 0.2, b, b + 0.2]$  with  $a$  and  $b$  being the values that give the smallest mean squared errors from the second iteration. In the fourth iteration, the sub-grid is refined to  $A = [a - 0.1, a, a + 0.1]$ ,  $B = [b - 0.1, b, b + 0.1]$ , where  $a$  and  $b$  are the parameters set with the smallest mean squared error from the third iteration. Finally, the parameter set with the smallest mean squared error from all the sub-grids will be adopted to be the density parameter of the supernova.

In this grid search strategy, a typical number of TARDIS models to be calculated is  $(9+8+8+8) \times N_{obs}$ , where 9, 8, 8, and 8 are the number of grid points in the four iterations described above, and  $N_{obs}$  is the number of observed spectra. For a well-observed SN with  $\sim 30$  spectra (e.g., SN 2005cf), the total computation time can exceed 1000 CPU hours. Therefore, we limit the number of observed spectra used in the grid search to about 10 based on the quality of the spectral data. For the well-observed SNe, we only select the spectra from ground-based telescopes with apertures larger than 3 meters in diameter and the Hubble Space Telescope (HST). The spectra are visually inspected to eliminate the data with obvious abnormal flux calibrations.

### 3. TESTING

#### 3.1. Error Estimate

In Figure 4, we use the neural network to predict the Ni abundance in Zone 3 using the testing data set, together with its associated predictive error ( $\sigma$ ). We notice when the predictive error is small, the predicted value is

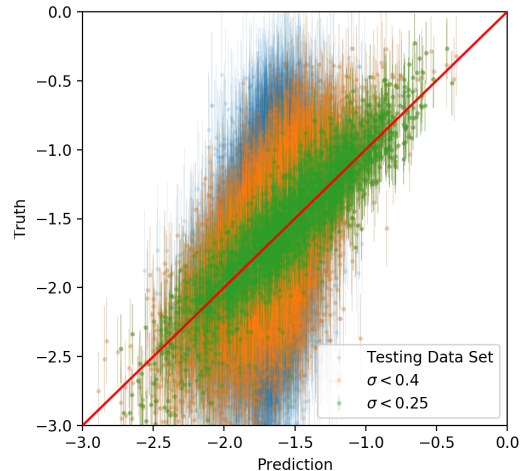


**Figure 4.** A comparison between the truth values and the predicted values of Ni abundance in Zone 3. The unit of both of the axes is the Ni mass fraction in logarithmic scale ( $\log_{10}(Ni)$ ). Data points with large predictive errors ( $\sigma \geq 0.4$ ) are in blue color, data points with medium predictive errors ( $0.4 > \sigma \geq 0.25$ ) are in orange color, data points with small predictive errors ( $\sigma < 0.25$ ) are in green color. A reference line (Prediction=Truth) is shown in red color. For illustration purposes, we only include 20000 data points randomly selected from the testing data set.

consistent with the true value. With increasing values of the predictive error, the predicted values systematically move away from the true values. When the predictive errors are larger than 0.4 dexes, the predicted values become insensitive to the truth values and take values in the range between -2.0 and -1.5. Therefore, we use  $\sigma$  as a criterion to measure the goodness of prediction on the observed spectra.

#### 3.2. Spectral Fitting

The parameters describing the density profile of the ejecta are determined from a grid search for the optimal values using Equation 4 for SN 2011fe. The optimal values of the parameter  $A$  and  $B$  are found to be 1.0 and 1.1, respectively. Figure 5 shows the elemental abundances derived from the observed spectral sequence of SN 2011fe. Figure 6 compares the best-fit spectra from the neural networks and the observed spectra.

We notice the spectra of SN 2011fe at 12.6 days, 16.59 days, 19.61 days, and 28.84 days show larger discrepancies in the UV than other epochs. Overall the quality of the spectral fits is worse in the ultraviolet than in the visible wavelength. This may be due to several reasons. First, the density profile used in this simulation is a simple exponential function which can be inappropriate for fitting the UV spectral region which is extremely sensi-

tive to the ejecta moving at high velocities. Secondly, the non-local thermodynamic equilibrium (NLTE) effect becomes more significant at the late time SNe Ia spectra, while TARDIS only uses nebula approximation to account for this effect. Thirdly, the assumption that all photons initiate from a sharp inner boundary is an over-simplification which can also affect the reliability of the models, especially in the UV. Nonetheless, the AIAI approach as adopted in this study makes it possible to derive model-based quantities that are sensitive to the chemical structures of the ejecta, although these derived quantities are dependent on the adopted models.

### 3.3. Ni Element Sensitivity

In this section, we use the SN ejecta structure predicted from the HST spectra of SN 2011fe at 12.6 days, 19.61 days, 22.89 days, 28.84 days to simulate 4 spectral sequences with different Ni abundance between 13000 – 17000  $km/s$  (Zone 3). In these models, we allow the mass fraction of Ni in Zone 3 to vary from  $10^{-4}$  to  $10^0$  while keeping the relative ratio of other elements in Zone 3 unchanged. Other model parameters such as the density structures are kept the same for all models. With this simulated spectral sequence, we employ the NNs constructed in the above section to derive the predicted elemental abundances. This serves as a test of the capability of the neural network in recovering the assumed model abundances before they can be applied to observational data. Figure 7 shows the predicted and the true Ni abundance in Zone 3 of the spectral sequences. The typical prediction errors are  $\sim 0.2$  dexes, and the predicted values are in general consistent with the truth when Ni abundance is larger than  $10^{-2.5}$  for the spectra in all four phases.

## 4. RESULTS

To identify the spectral lines from Ni, we apply our algorithm to the spectra of SN 2011fe at 19.61 days after the explosion taken by the Hubble Space Telescope (HST) to derive the chemical structure of the ejecta. Based on this ejecta structure, we artificially modify the elemental abundance in the velocity range between 13000 – 17000  $km/s$  (denoted as Zone 3) and the velocity range 10000 – 13000  $km/s$  (denoted as Zone 2) by changing the Ni fraction while re-scaling the abundances of the rest of the elements to keep the density profile conserved. Figure 8 shows the simulated spectra with Ni abundance in Zone 2 and 3 varying from  $10^{-4}$  to  $10^{-0.7}$  and  $10^{-4}$  to  $10^{-0.35}$ , respectively. We notice that Ni has a strong effect on the spectral features at 3750 – 3950 Å which can be attributed to the blueshifted absorption of the Ni II 4067 Å transition lines. This is the only line

in the optical in which the strength of Ni II absorption can be directly measured. This line is especially prominent when the Ni fraction is above  $10^{-2}$  in these velocity regions. Note also that the pseudo equivalent width (pEW) of the Si II absorption line at  $\sim 4000\text{Å}$  is affected by the Ni II transition lines. It has been shown in previous studies (Silverman et al. 2012; Walker et al. 2010) that the pseudo equivalent width (pEW) of the Si II absorption line at  $\sim 4000\text{Å}$  is correlated to the light curve stretch parameter and the absolute magnitude of SNe Ia. It is likely that the measurement of the pEW of the 4000 Å feature is capturing the combined effect of the Ni II and the Si II lines in this wavelength region.

Figure 7 shows the neural network predictions on the Ni abundance in Zone 3 based on a set of simulated spectra using the ejecta structure for the models of SN 2011fe, but with varying the Ni abundances in Zone 3. It can be seen that the predictions on the Ni abundance in Zone 3 are consistent with the truth values at different times after explosion for abundance values larger than  $\sim 10^{-2.5}$ . The linear relation is lost when the abundance drops below  $\sim 10^{-2.5}$ , indicating the sensitivity limit of the models. Figure 7 also shows an offset between the prediction and truth for day 12.6 which becomes less prominent at later epochs. We surmise the low Ni abundances are unable to produce spectral features stronger than the Monte-Carlo noise in the simulations, and that there are some hidden degeneracies in the model that are still not fully understood. A likely reason is that the electron scattering at zone 3 is still important at Zone 3 at the early epochs which reduces the sensitivity to Ni abundances in the spectral formation.

We focus on the flux ratio between the emission feature around 3950 Å and the absorption feature around 4000 Å, because the two spectral features can be identified in most of the SNe Ia optical spectra, and the wavelength range is small such that the flux ratio is less affected by the dust extinction effect. Firstly, we measure the flux of the local minimum close to 4000 Å and define the minimal flux as  $F_{\lambda 4000}$ . Then, we measure the nearest local maximum flux to the blue-side of the local minimum and define the local maximum flux as  $F_{\lambda 3950}$ . Finally, we define the flux ratio  $FRNi = F_{\lambda 3950}/F_{\lambda 4000}$ , and use this  $FRNi$  as a spectral indicator that can be related to the Ni abundances.

We searched all the available SNe Ia spectra from WISeREP (Yaron & Gal-Yam 2012) and kaepora (Siebert et al. 2019) and found 616 spectra from 153 SNe Ia, which were observed between -10 days and 20 days relative to the B-band maximum time with the rest frame wavelength covering 3800 – 7000 Å, for our analysis. We also collected the  $\Delta m_{15}$  parameters of these

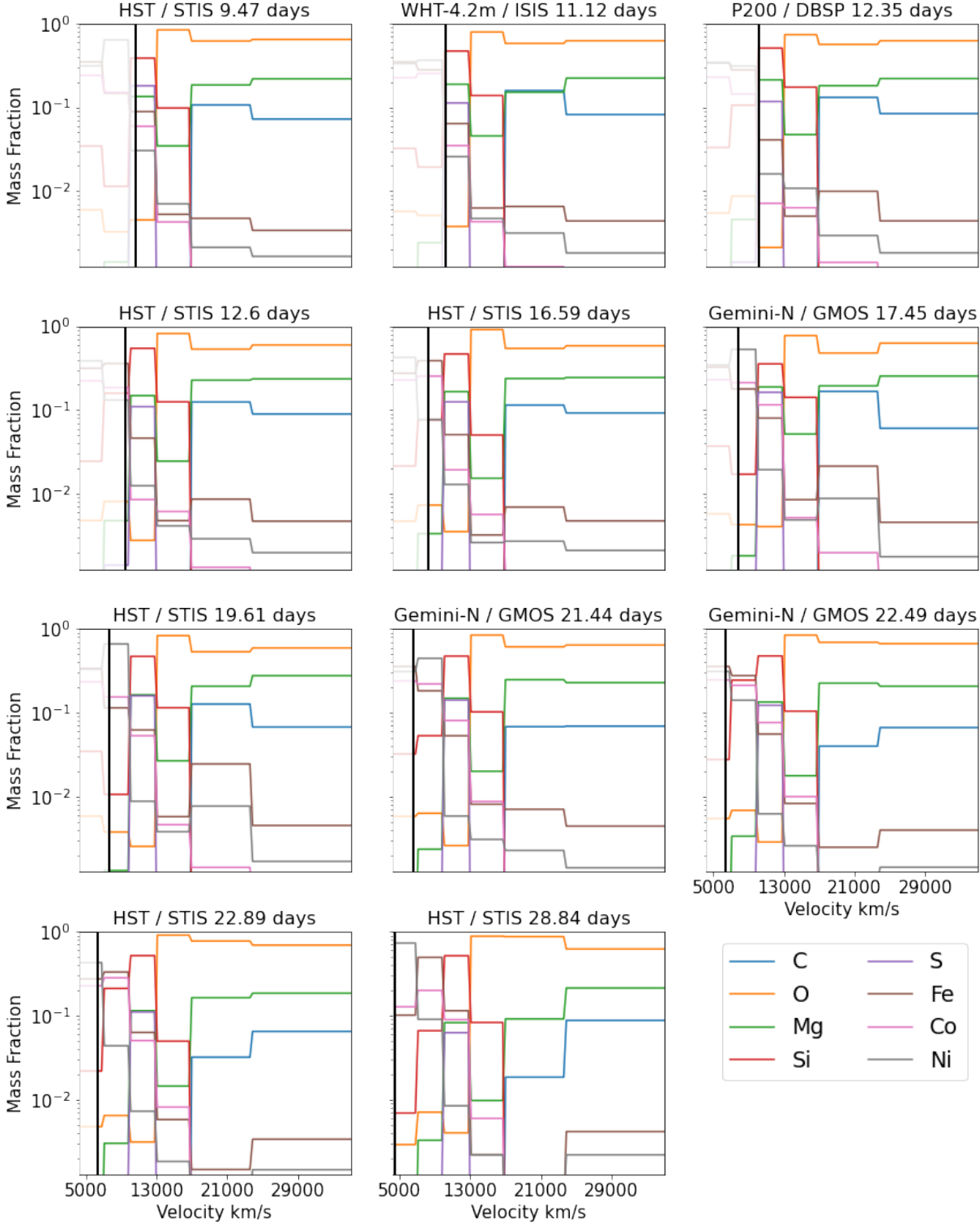


**Figure 5.** The element abundance time sequence predicted from the SN2011fe spectra with density parameters  $A = 1.0$  and  $B = 1.1$ . The sources of the data and the time after the explosions are shown as panel titles. The thick vertical black lines mark the velocities of the inner boundary which are also one of the parameters predicted by applying the neural networks to the observed spectra. Elemental abundances below the inner boundaries are insensitive to the observations of their corresponding epochs.



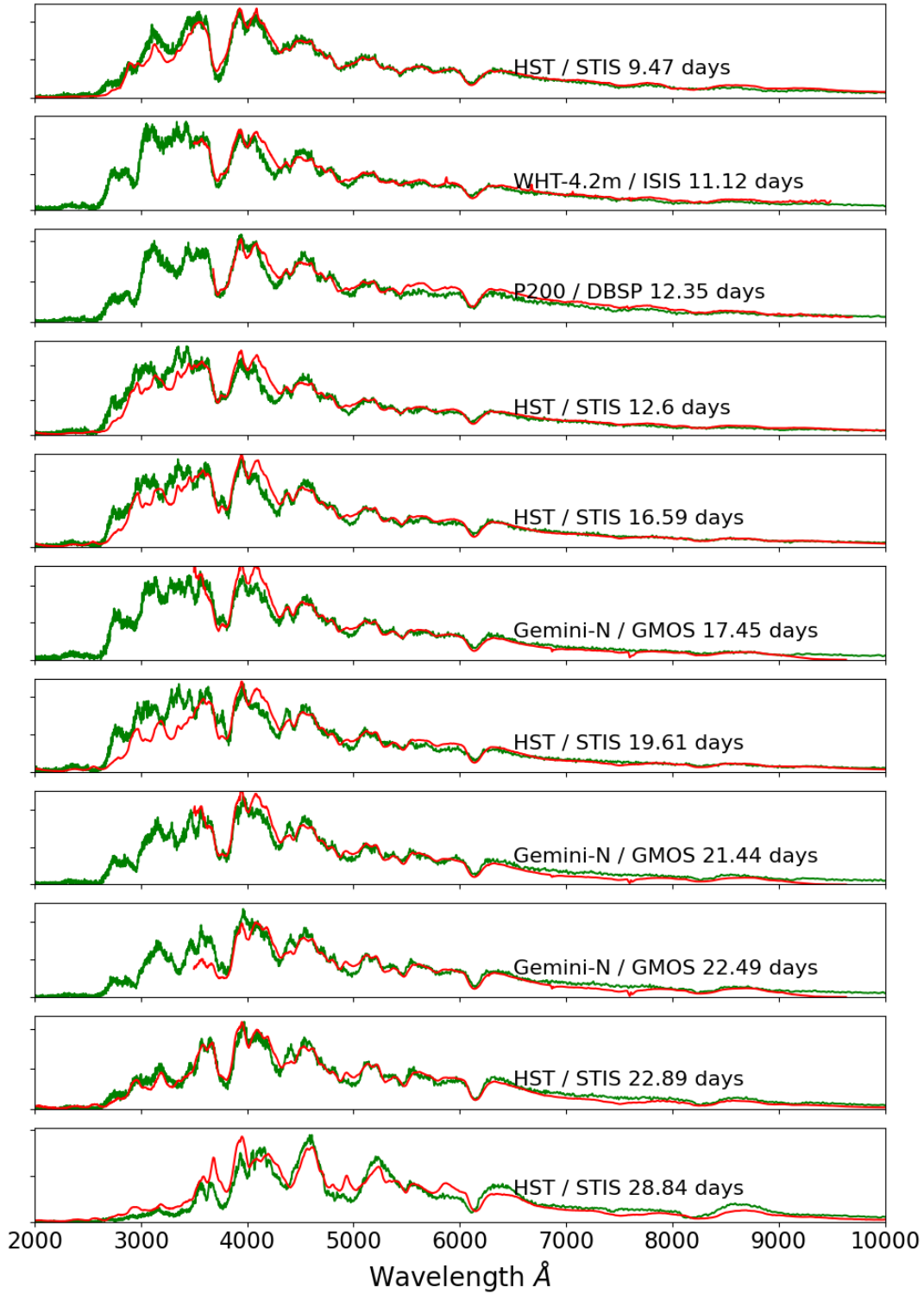


**Figure 6.** A comparison of the simulated spectra (green lines) using the density parameters  $A = 1.0$ ,  $B = 1.1$ , and the observed spectra (red lines) of SN 2011fe. The sources of the data and the epochs after the explosion are shown above the data of each epoch. All the observed spectra are de-redshifted and with Milky Way and host galaxy dust removed as in [kaepora](#) (Siebert et al. 2019).

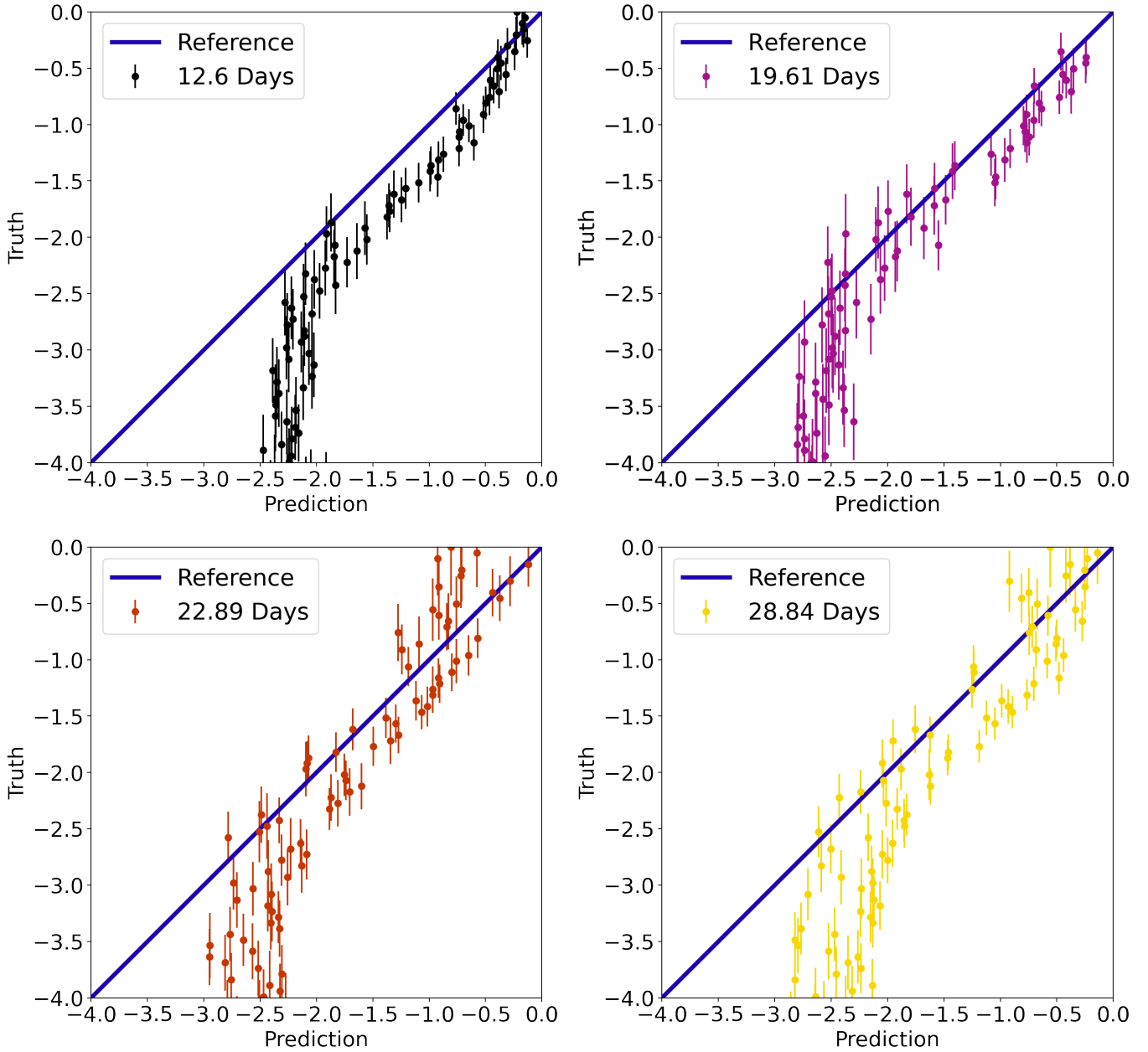


**Figure 7.** The predicted value compared to the truth value of the neural network. The horizontal and vertical axes show the Truths and Predictions, respectively, of the logarithmic Ni mass fraction  $\log_{10}(Ni)$  in the velocity range  $13000 - 17000 km/s$  (Zone 3). The spectra used for these predictions are generated from TARDIS based on the ejecta structure derived for SN 2011fe but varying the Ni mass fraction in the velocity range  $13000 - 17000 km/s$ . The blue lines show Prediction = Truth. The times after the explosion of the simulated spectra are labeled in the upper left of each figure.

SNe from kaepora Siebert et al. (2019) or calculated the  $\Delta m_{15}$  parameter using the light curves from kaepora Siebert et al. (2019) or Open Supernova Catalog<sup>1</sup>. All the spectra are converted to rest frame and corrected for dust extinction effects using the data from kaepora Siebert et al. (2019). The times after the explosion of

these SNe are calculated assuming the  $B$ -band maximum time is 19 days after the explosion. Moreover, because the inner boundary velocity of TARDIS falls in Zone 2 for most of the SN models at the epochs between  $-10$  and  $0$  days relative to their  $B$ -band maximum, we will only use the Ni abundance in Zone 3 which is less affected by the location of the TARDIS inner boundary for the early-phase spectral models as measures of Ni abundances when comparing models with observations.

<sup>1</sup> <https://sne.space/>

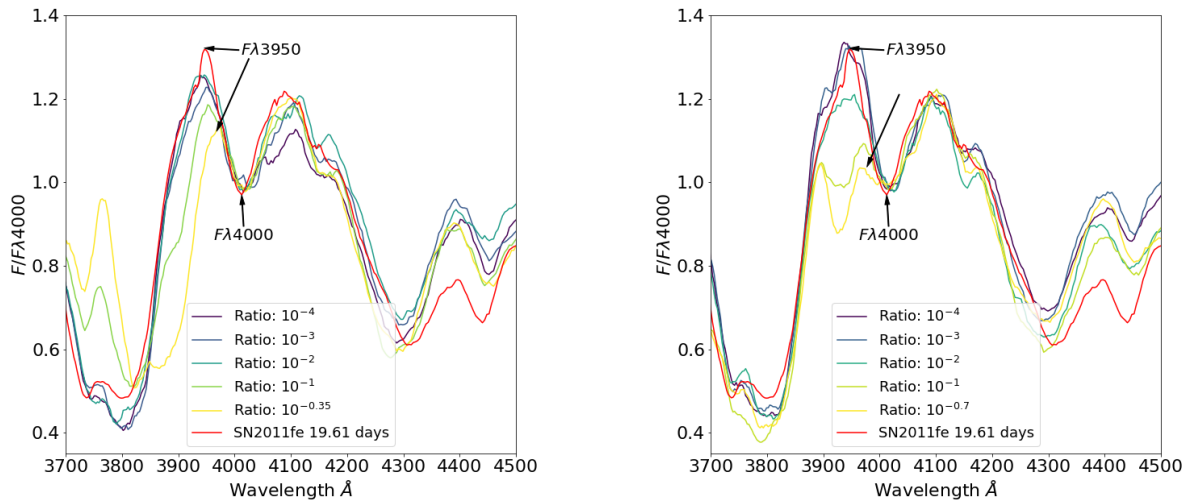


**Figure 8.** An illustration of measuring the spectral line flux ratio  $FRNi$ . The red lines are the spectra of SN2011fe at 19.61 days after the explosion. The lines of the different colors are the simulated spectra using TARDIS. The simulated spectra on the left and right are computed with varying Ni mass fractions in the velocity ranges 13000 – 17000 km/s (Zone 3) and 10000 – 13000 km/s (Zone 2), respectively. The Ni mass fractions are shown in the legends of the two figures. All the spectra are normalized to the local minimum flux near 4000Å. The black arrows indicate the local minimum and maximum that are used to measure the spectral line flux ratio  $FRNi = F(\lambda 3950)/F(\lambda 4000)$ .

In Figure 9, we show the relation between  $\Delta m_{15}$  and the Ni abundance in Zone 3 of the selected SNe. The Figure shows clear correlations between  $\Delta m_{15}$  and the derived Ni mass fraction in Zone 3 for the spectra between 9 and 12 days and between 12 and 15 days after the explosion. The correlation is much weaker in the data between 15 and 18 days after the explosion, as the Ni abundances are significantly lower than in earlier epochs and for most of the SNe they are close to the detection limit. The Ia-99aa subtype SNe and the Ia-91T subtype SNe are found in the regions with larger Ni mass fraction and smaller  $\Delta m_{15}$ . The Ia-91bg subtype SNe shows large  $\Delta m_{15}$  and low Ni mass fraction, consistent with them being underluminous due to the deficiency of  $^{56}Ni$  in the ejecta as the source of energy. The Iax subtype SNe are comparatively isolated from the rest of the SNe Ia, showing large  $\Delta m_{15}$  and large Ni mass fraction. Moreover, the Ni abundance in Zone 3 does not show a significant decrease for type Iax SNe. If confirmed by observations and models, this indicates that the Ni in Type Iax may be primarily stable isotopes of Ni.

The relation between the Ni abundances in Zone 3 and the spectral line ratio  $FRNi$  is shown in Figure 10. We notice  $FRNi$  shows a linear correlation to the logarithmic Ni abundance in Zone 3  $\log_{10}(Ni)$ , especially for the spectra between 12 and 15 days. Such a linear correlation is weaker for the spectra between the phase

15 and 18 days, probably because the Ni abundances have decreased below the detection limit for most of the SNe. The Ia-99aa and Ia-91T subtype SNe show higher Ni abundances and lower  $FRNi$  parameters compared to spectroscopically normal SNe Ia. The Ia-91bg subtype SNe show lower Ni abundances and large  $FRNi$  parameters.

In Figure 11, we show the time evolution of the Ni abundance in Zone 3 for SN 2011fe, SN 2005cf, SN 2013dy, ASASSN-14lp, SN 2014J, and SN 2015F. The Ni abundances in SN 2011fe and SN 2015F are close to the detection limit, and only SN 2011fe shows the signal of Ni at an early phase. SN 2005cf shows a distinct decay of Ni abundance in Zone 3 and the decay rate is slightly larger than the  $^{56}Ni$  decay rate. The overluminous SN 2013dy and ASASSN-14lp exhibit high Ni abundance in Zone 3, while the Ni abundance decay is not obvious due to inadequate data quality and poor sampling time. SN 2014J shows a Ni abundance as high as SN 2013dy or ASASSN-14lp, and the Ni abundance decay trend is observed between 15 – 20 days after the explosion, but the data before day 14 show a large scatter.

## 5. CONCLUSION

We employ the program TARDIS to build a set of NNs to calculate the Ni element in SN Ia ejecta. We measure the Ni abundances and their time evolution in the 13000 - 17000 km/s region of 153 SNe Ia, and correlate the

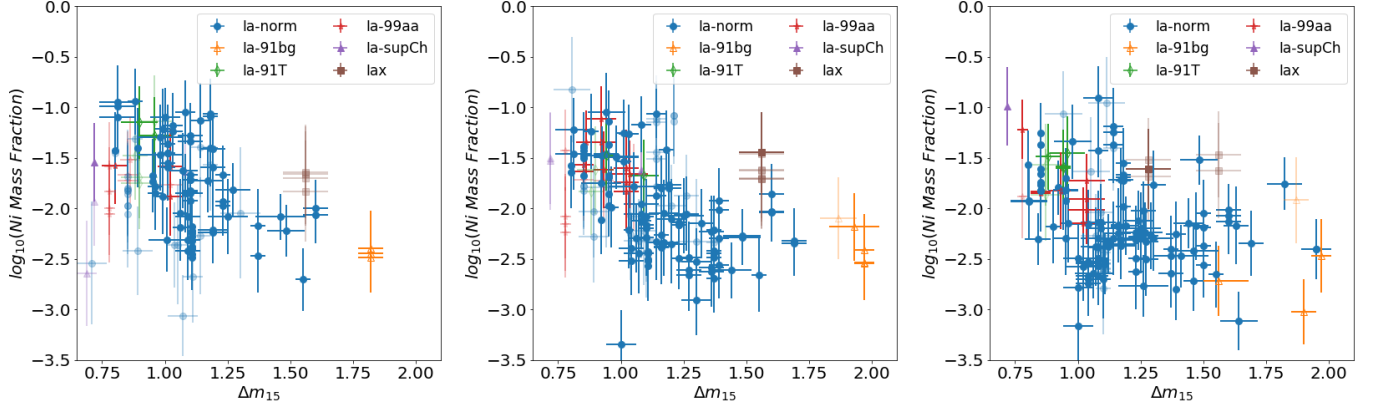


**Figure 9.** The relation between  $\Delta m_{15}$  and the Ni abundance in Zone 3 at different time bins. Left panel: between 9 and 12 days from the time of the explosion. Middle panel: between 12 and 15 days from the time of the explosion. Right panel: between 15 and 18 days from the time of the explosion.  $y$ -axis is the Ni mass fraction in Zone 3 in the logarithmic scale. Spectroscopically normal SNe Ia are marked with blue solid circles, Ia-91bg-like SNe are marked with orange hollow triangles, Ia-91T-like SNe are marked with green diamonds, Ia-99aa-like SNe are marked with red solid stars, Ia-super-Chandrasekar SNe are marked with purple solid triangles, and Iax SNe are marked with brown squares. Data points with large errors on the  $y$ -axis ( $\sigma > 0.4$ ) are transparent.

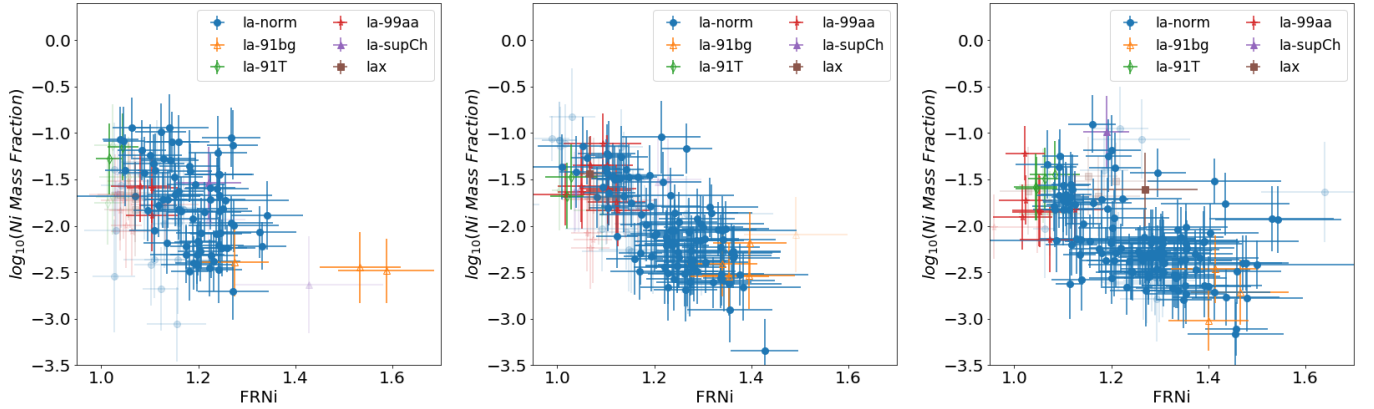


**Figure 10.** The relation between the spectral line ratio ( $FRNi$ ) measured from the observed spectra of SNe and the Ni abundance in Zone 3 determined by applying the neural network models to the observed data. The three panels are for observations in different time windows after the explosion. Left panel: between 9 and 12 days after the explosion. Middle panel: between 12 and 15 days after the explosion. Right panel: between 15 and 18 days after the explosion. The vertical axes show the Ni mass fraction in Zone 3 on a logarithmic scale. Different subtypes of SNe Ia are labeled with different colors and marks, the color and mark encodings are the same as Figure 9. Data points with large errors on the vertical axis ( $\sigma > 0.4$ ) are transparent. This figure includes the following sub-Types of SNe Ia: normal (blue), SN 1991bg-like (orange), SN 1991T-like (green), SN 1999aa-like (red), super-Chandrasekhar (purple), and Iax (brown).

Ni abundance to the spectral feature around  $3950 \text{ \AA}$  and the supernova light curve parameter  $\Delta m_{15}$ . The neural network prediction on the Ni in the 13000 - 17000 km/s region can reach 0.2 dex accuracy on the simulated SN 2011fe spectra, and the sensitivity can reach  $10^{-2.5}$  of Ni mass fraction. On the observed spectra, we found the predictive error of most of the predictions is smaller than 0.4 dex, and the predicted Ni abundance is loosely correlated to the nickel spectral line feature  $FRNi$  and the light curve parameter  $\Delta m_{15}$ , especially in the early phase spectra, probably due to more  $^{56}Ni$  exists in the

early phase SNe Ia ejecta. The Ni spectral line features  $FRNi$ , and the ejecta structures predicted by the neural network could be further used in cosmological studies to estimate the  $H_0$  value more accurately.

We also notice the simulated spectra based on the neural network predictions do not perfectly fit the observations, especially in the ultraviolet wavelength. Moreover, the Ni abundance evolution of several well-observed SNe only loosely observes the theoretical  $^{56}Ni$  decay curve. We surmise these defects could be due to the crude approximation of NLTE calculation in the radi-

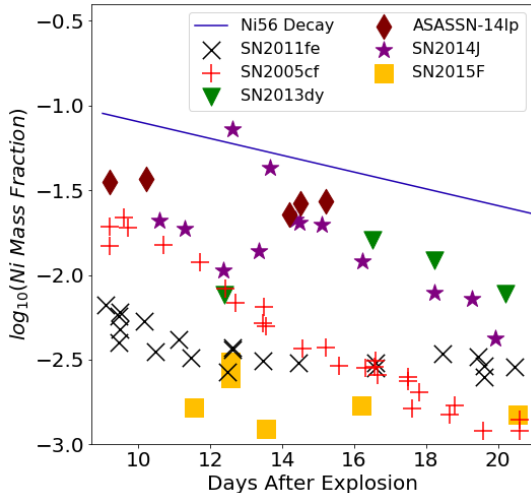


**Figure 11.** The Ni abundance evolution with time after SN explosion for different SNe Ia. Y axis is the Ni mass fraction in Zone 3 on a logarithmic scale. The ultramarine line is the theoretical  $^{56}\text{Ni}$  abundance changing with time. Six well-observed type Ia-normal SNe: SN2011fe (black cross), SN2005cf (red plus), SN2013dy (green triangle), ASASSN-14lp (brown diamond), SN2014J (purple star), SN2015F (yellow square) are shown with different markers.

tive transfer simulation program TARDIS, and the oversimplification of the theoretical SN ejecta density profile. The deviation of TARDIS model from Sedona and CM-FGEN is found to be the largest in the UV wavelength range (see Fig. 12 in, Blondin et al. 2022). The TARDIS code generates photons from an inner boundary, and the other part of the ejecta only reprocess photons from the inner boundary. Sedona made the improvement of more realistically generating photons in the Monte-Carlo simulation, but Sedona models are much more costly to compute.

With AI, it is possible to ‘calibrate’ codes with simplified approximations to make them agree with results from codes with more complete treatments of physical processes. The physical model-based parametrization of the observational data of SNe Ia as developed in this study can be extended to include other radiative transfer codes (e.g., Hoefflich et al. 1996; Hillier & Miller 1998; Baron & Hauschildt 1998; Kasen et al. 2006). Such parametrization is different from what has been done so far based on empirical models of SN Ia luminosity-distance relations (e.g., Phillips 1993; Tripp 1998; Jha et al. 2007; Guy et al. 2005; Wang et al. 2003b, 2006). For future projects of supernova cosmology, the theoretical model-based parametrization has a different sensitivity to the systematic errors of supernova evolution, it may prove to be important for controlling the systematic evolutions of the age and metallicity of SN Ia progen-

itors, especially when very high redshift ( $z \sim 3 - 6$ ) SNe Ia are involved (Lu et al. 2022).

It is also important to have a fast code to generate surrogate models of 3-D radiative transfer to account for the asymmetric geometry of the ejecta as found from spectropolarimetry observations (Wang et al. 1996; Wang & Wheeler 2008; Cikota et al. 2019; Yang et al. 2022b) and theoretical models (e.g., Neopane et al. 2022). These works will be reported in a forthcoming study (Chen et al. in prep.).

1 Portions of this research were conducted with the ad-  
 2 vanced computing resources provided by Texas A&M  
 3 High-Performance Research Computing. This research  
 4 used resources of the National Energy Research Sci-  
 5 entific Computing Center (NERSC), a U.S. Depart-  
 6 ment of Energy Office of Science User Facility oper-  
 7 ated under Contract No. DE-AC02-05CH11231. LW  
 8 acknowledges the NSF grant AST-1817099 for support  
 9 on this work. This paper made use of `netron`, an  
 10 open-source program for neural network visualization  
 11 <https://github.com/lutzroeder/netron>. This research  
 12 used TARDIS, a community-developed software pack-  
 13 age for spectral synthesis in supernovae Kerzendorf &  
 14 Sim (2014); Kerzendorf et al. (2020). The development  
 15 of TARDIS received support from the Google Summer of  
 16 Code initiative and from ESA’s Summer of Code in the  
 17 Space program. TARDIS makes extensive use of Astropy  
 18 and PyNE.

## REFERENCES

- Abdi, M., & Nahavandi, S. 2016, *CoRR*, abs/1609.05672.  
<https://arxiv.org/abs/1609.05672>
- Aldoroty, L., Wang, L., Hoeflich, P., et al. 2022, arXiv  
 e-prints, arXiv:2210.06708.  
<https://arxiv.org/abs/2210.06708>
- Arnett, W. D. 1982, *ApJ*, 253, 785, doi: [10.1086/159681](https://doi.org/10.1086/159681)
- Baron, E., & Hauschildt, P. H. 1998, *The Astrophysical  
 Journal*, 495, 370, doi: [10.1086/305287](https://doi.org/10.1086/305287)
- Blondin, S., Blinnikov, S., Callan, F. P., et al. 2022, arXiv  
 e-prints, arXiv:2209.11671.  
<https://arxiv.org/abs/2209.11671>
- Bulla, M., Sim, S. A., & Kromer, M. 2015, *MNRAS*, 450,  
 967, doi: [10.1093/mnras/stv657](https://doi.org/10.1093/mnras/stv657)
- Bulla, M., Sim, S. A., Kromer, M., et al. 2016, *Monthly  
 Notices of the Royal Astronomical Society*, 462, 1039,  
 doi: [10.1093/mnras/stw1733](https://doi.org/10.1093/mnras/stw1733)
- Chen, X., Hu, L., & Wang, L. 2020, *The Astrophysical  
 Journal Supplement Series*, 250, 12,  
 doi: [10.3847/1538-4365/ab9a3b](https://doi.org/10.3847/1538-4365/ab9a3b)
- Childress, M. J., Hillier, D. J., Seitzzahl, I., et al. 2015,  
*MNRAS*, 454, 3816, doi: [10.1093/mnras/stv2173](https://doi.org/10.1093/mnras/stv2173)
- Cikota, A., Patat, F., Wang, L., et al. 2019, *MNRAS*, 490,  
 578, doi: [10.1093/mnras/stz2322](https://doi.org/10.1093/mnras/stz2322)
- Guy, J., Astier, P., Nobili, S., Regnault, N., & Pain, R.  
 2005, *A&A*, 443, 781, doi: [10.1051/0004-6361:20053025](https://doi.org/10.1051/0004-6361:20053025)
- Hauschildt, P. H., & Baron, E. 2006, *A&A*, 451, 273,  
 doi: [10.1051/0004-6361:20053846](https://doi.org/10.1051/0004-6361:20053846)
- Hillier, D. J., & Miller, D. L. 1998, *ApJ*, 496, 407,  
 doi: [10.1086/305350](https://doi.org/10.1086/305350)
- Hoeflich, P., Khokhlov, A., Wheeler, J. C., et al. 1996, *The  
 Astrophysical Journal Letters*, 472, L81,  
 doi: [10.1086/310363](https://doi.org/10.1086/310363)
- Höflich, P. 1991, *A&A*, 246, 481
- Hsiao, E. Y., Conley, A., Howell, D. A., et al. 2007, *The  
 Astrophysical Journal*, 663, 1187, doi: [10.1086/518232](https://doi.org/10.1086/518232)
- Hu, L., Chen, X., & Wang, L. 2022, *ApJ*, 930, 70,  
 doi: [10.3847/1538-4357/ac5c48](https://doi.org/10.3847/1538-4357/ac5c48)
- Jha, S., Riess, A. G., & Kirshner, R. P. 2007, *ApJ*, 659,  
 122, doi: [10.1086/512054](https://doi.org/10.1086/512054)
- Kasen, D., Thomas, R. C., & Nugent, P. 2006, *ApJ*, 651,  
 366, doi: [10.1086/506190](https://doi.org/10.1086/506190)
- Kasen, D., Nugent, P., Wang, L., et al. 2003, *ApJ*, 593, 788,  
 doi: [10.1086/376601](https://doi.org/10.1086/376601)
- Kerzendorf, W., Sim, S., Vogl, C., et al. 2020,  
 tardis-sn/tardis: TARDIS v3.0.dev3459, v3.0.dev3459,  
 Zenodo, doi: [10.5281/zenodo.3893940](https://doi.org/10.5281/zenodo.3893940)
- Kerzendorf, W. E., & Sim, S. A. 2014, *Monthly Notices of  
 the Royal Astronomical Society*, 440, 387,  
 doi: [10.1093/mnras/stu055](https://doi.org/10.1093/mnras/stu055)
- Kerzendorf, W. E., Vogl, C., Buchner, J., et al. 2020, arXiv  
 e-prints, arXiv:2007.01868.  
<https://arxiv.org/abs/2007.01868>
- Khatami, D. K., & Kasen, D. N. 2019, *ApJ*, 878, 56,  
 doi: [10.3847/1538-4357/ab1f09](https://doi.org/10.3847/1538-4357/ab1f09)

- Kingma, D. P., & Ba, J. 2014, CoRR, abs/1412.6980.  
<https://arxiv.org/abs/1412.6980>
- Krizhevsky, A., Sutskever, I., & Hinton, G. E. 2012, in Advances in Neural Information Processing Systems 25, ed. F. Pereira, C. J. C. Burges, L. Bottou, & K. Q. Weinberger (Curran Associates, Inc.), 1097–1105.  
<http://papers.nips.cc/paper/4824-imagenet-classification-with-deep-convolutional-neural-networks.pdf>
- Kromer, M., & Sim, S. A. 2009, Monthly Notices of the Royal Astronomical Society, 398, 1809,  
 doi: [10.1111/j.1365-2966.2009.15256.x](https://doi.org/10.1111/j.1365-2966.2009.15256.x)
- Lakshminarayanan, B., Pritzel, A., & Blundell, C. 2016, arXiv e-prints, arXiv:1612.01474.  
<https://arxiv.org/abs/1612.01474>
- Lecun, Y., Bengio, Y., & Hinton, G. 2015, Nature, 521, 436,  
 doi: [10.1038/nature14539](https://doi.org/10.1038/nature14539)
- Livneh, R., & Katz, B. 2022, MNRAS,  
 doi: [10.1093/mnras/stab3787](https://doi.org/10.1093/mnras/stab3787)
- Lu, J., Wang, L., Chen, X., et al. 2022, arXiv e-prints, arXiv:2210.00746. <https://arxiv.org/abs/2210.00746>
- Lucy, L. B. 1999, Astronomy and Astrophysics, 345, 211
- Lucy, L. B. 2002, A&A, 384, 725,  
 doi: [10.1051/0004-6361:20011756](https://doi.org/10.1051/0004-6361:20011756)
- . 2003, A&A, 403, 261, doi: [10.1051/0004-6361:20030357](https://doi.org/10.1051/0004-6361:20030357)
- Mazzali, P. A., & Lucy, L. B. 1993, Astronomy and Astrophysics, 279, 447
- Neopane, S., Bhargava, K., Fisher, R., et al. 2022, ApJ, 925, 92, doi: [10.3847/1538-4357/ac3b52](https://doi.org/10.3847/1538-4357/ac3b52)
- Parrent, J., Branch, D., & Jeffery, D. 2010, SYNOW: A Highly Parameterized Spectrum Synthesis Code for Direct Analysis of SN Spectra. <http://ascl.net/1010.055>
- Phillips, M. M. 1993, The Astrophysical Journal Letters, 413, L105, doi: [10.1086/186970](https://doi.org/10.1086/186970)
- Piro, A. L., Chang, P., & Weinberg, N. N. 2010, ApJ, 708, 598, doi: [10.1088/0004-637X/708/1/598](https://doi.org/10.1088/0004-637X/708/1/598)
- Piro, A. L., & Morozova, V. S. 2016, ApJ, 826, 96,  
 doi: [10.3847/0004-637X/826/1/96](https://doi.org/10.3847/0004-637X/826/1/96)
- Röpke, F. K. 2005, A&A, 432, 969,  
 doi: [10.1051/0004-6361:20041700](https://doi.org/10.1051/0004-6361:20041700)
- Röpke, F. K., Kromer, M., Seitzzahl, I. R., et al. 2012, ApJL, 750, L19, doi: [10.1088/2041-8205/750/1/L19](https://doi.org/10.1088/2041-8205/750/1/L19)
- Rubin, D., Knop, R. A., Rykoff, E., et al. 2013, The Astrophysical Journal, 763, 35,  
 doi: [10.1088/0004-637x/763/1/35](https://doi.org/10.1088/0004-637x/763/1/35)
- Siebert, M. R., Foley, R. J., Jones, D. O., et al. 2019, Monthly Notices of the Royal Astronomical Society, 486, 5785, doi: [10.1093/mnras/stz1209](https://doi.org/10.1093/mnras/stz1209)
- Silverman, J. M., Ganeshalingam, M., Li, W., & Filippenko, A. V. 2012, Monthly Notices of the Royal Astronomical Society, 425, 1889, doi: [10.1111/j.1365-2966.2012.21526.x](https://doi.org/10.1111/j.1365-2966.2012.21526.x)
- Simonyan, K., & Zisserman, A. 2014, arXiv e-prints, arXiv:1409.1556. <https://arxiv.org/abs/1409.1556>
- Stehle, M., Mazzali, P. A., Benetti, S., & Hillebrandt, W. 2005, MNRAS, 360, 1231,  
 doi: [10.1111/j.1365-2966.2005.09116.x](https://doi.org/10.1111/j.1365-2966.2005.09116.x)
- Thomas, R. C., Nugent, P. E., & Meza, J. C. 2011, PASP, 123, 237, doi: [10.1086/658673](https://doi.org/10.1086/658673)
- Townsley, D. M., Miles, B. J., Shen, K. J., & Kasen, D. 2019, The Astrophysical Journal, 878, L38,  
 doi: [10.3847/2041-8213/ab27cd](https://doi.org/10.3847/2041-8213/ab27cd)
- Tripp, R. 1998, A&A, 331, 815
- Walker, E. S., Hook, I. M., Sullivan, M., et al. 2010, Monthly Notices of the Royal Astronomical Society, 410, 1262, doi: [10.1111/j.1365-2966.2010.17519.x](https://doi.org/10.1111/j.1365-2966.2010.17519.x)
- Wang, L., Goldhaber, G., Aldering, G., & Perlmutter, S. 2003a, The Astrophysical Journal, 590, 944,  
 doi: [10.1086/375020](https://doi.org/10.1086/375020)
- . 2003b, The Astrophysical Journal, 590, 944,  
 doi: [10.1086/375020](https://doi.org/10.1086/375020)
- Wang, L., Strovink, M., Conley, A., et al. 2006, The Astrophysical Journal, 641, 50, doi: [10.1086/500422](https://doi.org/10.1086/500422)
- Wang, L., & Wheeler, J. C. 2008, ARA&A, 46, 433,  
 doi: [10.1146/annurev.astro.46.060407.145139](https://doi.org/10.1146/annurev.astro.46.060407.145139)
- Wang, L., Wheeler, J. C., Li, Z., & Clocchiatti, A. 1996, ApJ, 467, 435, doi: [10.1086/177617](https://doi.org/10.1086/177617)
- Wilk, K. D., Hillier, D. J., & Dessart, L. 2017, Monthly Notices of the Royal Astronomical Society, 474, 3187,  
 doi: [10.1093/mnras/stx2816](https://doi.org/10.1093/mnras/stx2816)
- Woosley, S. E., Kasen, D., Blinnikov, S., & Sorokina, E. 2007, ApJ, 662, 487, doi: [10.1086/513732](https://doi.org/10.1086/513732)
- Yang, J., Wang, L., Suntzeff, N., et al. 2022a, ApJ, 938, 83,  
 doi: [10.3847/1538-4357/ac8c97](https://doi.org/10.3847/1538-4357/ac8c97)
- Yang, Y., Yan, H., Wang, L., et al. 2022b, arXiv e-prints, arXiv:2208.12862. <https://arxiv.org/abs/2208.12862>
- Yaron, O., & Gal-Yam, A. 2012, Publications of the Astronomical Society of the Pacific, 124, 668,  
 doi: [10.1086/666656](https://doi.org/10.1086/666656)